Applied Physics Express 7, 105501 (2014)
http://dx.doi.org/10.7567/APEX.7.105501

Plasma MBE growth conditions of AlGaN/GaN high-electron-mobility transistors on silicon and their device characteristics with epitaxially regrown ohmic contacts

Satyaki Ganguly*, Jai Verma, Huili (Grace) Xing, and Debdeep Jena

Department of Electrical Engineering, University of Notre Dame, Notre Dame, IN 46556, U.S.A.

Received July 7, 2014; accepted August 25, 2014; published online September 11, 2014

Silicon substrates offer an attractive substrate platform for GaN RF and power electronics. In this work, we address the key challenges and provide solutions for the RF-MBE growth of GaN high-electron-mobility transistors (HEMTs) on Si(111). Moreover, by developing low-leakage buffer layers and employing raised source/drain regrown ohmic contacts, high-performance HEMTs are realized at a significantly lower process temperature by plasma MBE than by MOCVD. This is expected to motivate further ideas for the integration of GaN with silicon that go beyond RF and power electronics into the regime of low-power digital logic by exploiting the unique polarization properties of GaN.
© 2014 The Japan Society of Applied Physics

Owing to the limited availability of native bulk III–nitride semiconductor substrates, SiC and sapphire have been traditionally used as substrates for III–nitride high-electron-mobility transistors (HEMTs).[1] The high thermal conductivity and small lattice mismatch with III–nitrides make SiC a good choice for HEMTs leading to record performance.[2] Growth on silicon, however, permits the functional integration of high-voltage and RF nitride HEMTs with Si complementary metal–oxide–semiconductor (CMOS) technology.[3,4] Interestingly, it can also be seen as a precursor to the potential use of the unique polarization properties of III–nitrides for *low-power* digital logic as well. For example, recently, the inherent feedback mechanism in the piezoelectric nature of III–nitride gate barriers has been proposed as a mechanism leading to sub-60 mV/decade steep switching.[5] A recent report has provided experimental demonstration of sub-60 mV/decade switching in a III–nitride HEMT.[6]

Since the first successful demonstration of the growth of high-quality GaN on Si(111) by MOCVD using a high-temperature AlN nucleation layer,[7] attractive results have been reported for GaN HEMTs grown by MOCVD[8] as well as by MBE.[9,10] MBE growth provides the opportunity for lower temperatures and also the regrowth process for ultralow contact resistances. In this work, we address the key challenges specific to the GaN HEMT growth on Si by MBE and provide solutions that result in high-performance AlGaN/GaN HEMTs suitable for both digital and RF applications. Our sheet resistance (R_{sh}) of the two-dimensional electron gas (2DEG) channel indicating the transport properties and the full width at half maximum (FWHM) of the GaN indicating the structural properties are among the lowest reported to date by MBE growth.

MBE-regrown contacts[11] have been employed recently in GaN HEMTs for reducing losses in parasitic resistances, resulting in a performance boost in metal- and N-polar HEMTs on SiC.[12,13] For GaN HEMTs on Si, a low contact resistance R_c of ~0.27 Ω·mm by MOCVD has recently been reported.[14] This is higher than those achieved by MBE regrowth, presumably owing to the different growth regimes. In this work, we present the detailed process steps and interface analysis of the MBE-regrown n+ GaN and AlGaN barrier. The resulting R_c of ~0.1 Ω·mm is the lowest reported for GaN HEMTs on Si. The performance boost of the GaN HEMTs on Si with the regrown contact as compared with the annealed contact is discussed. The low-resistance MBE-regrown contact technology reduces losses in high-power and high-frequency microwave applications, and mitigates the problem of the low thermal conductivity of Si compared with that of SiC.

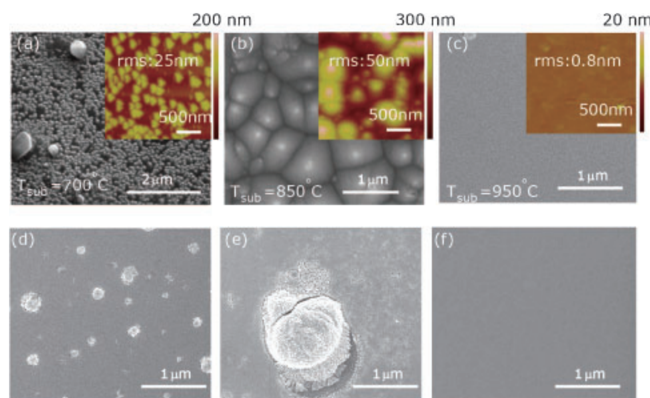

Fig. 1. (a–c) SEM images of the surface of AlN nucleation layers grown by MBE on Si(111) at various substrate temperatures. Higher growth temperatures led to a smooth 2D surface morphology. The corresponding AFM scans are shown in the inset. (d–f) Top-view SEM images of the corresponding AlGaN/GaN HEMTs using the same AlN nucleation layer growth condition as in (c). (d–e) Unoptimized fluxes destroy the grown epilayer surface in a large scale. Optimal growth leads to a smooth surface morphology, as shown in (f).

AlN has been traditionally used as an interlayer to grow high-quality GaN on Si(111). The role of the AlN seed layer is to structurally decouple the top GaN layer from the underlying Si substrate. The AlN layer induces a compressive stress in the subsequently grown GaN layers, partially counterbalancing both the growth and the thermally induced tensile stress, thus avoiding cracking. In this work, a set of samples with 120 nm AlN nucleation layers were grown on 3-in. (111) high-resistivity (HR) Si wafers of $\rho > 10^4$ Ω·cm. The substrate thermocouple temperature T_{sub} was varied from 700 to 950 °C, keeping all other growth parameters identical at an RF power of ~400 W and an Al flux of $\sim 1 \times 10^{-7}$ Torr. For T_{sub} of ~700 °C, the AlN grew in the form of three-dimensional (3D) islands. With the increase in T_{sub}, the islands coalesced, and at T_{sub} of ~950 °C, a smooth two-dimensional (2D) AlN surface was obtained, as shown in Figs. 1(a)–1(c). The 2×2 RHEED reconstruction observed during growth confirmed the metal polarity of the epilayer. The 120-nm-thick crack-free metal polar AlN film grown at an RF power of ~400 W and T_{sub} of ~950 °C with ~0.8 nm rms roughness over $2 \times 2\,\mu m^2$ atomic force microscopy (AFM) scans resulted in an FWHM of 42 arcmin, one of the

© 2014 The Japan Society of Applied Physics

lowest reported[15] so far. This nucleation condition was used for the subsequent growth of HEMTs as discussed next.

A series of metal-polar $Al_{0.32}Ga_{0.68}N$ (~22 nm)/GaN (600–800 nm)/AlN (100 nm)/Si(111) samples were grown by varying Al/Ga fluxes and substrate temperature to determine the optimal HEMT growth conditions. It was found that the surface morphologies of these structures were very sensitive to the Al/Ga fluxes. Unoptimized, excess Ga flux (Ga flux $\gg$ N flux) can create chunks of microcrystals, destroying the 2D nature of the AlGaN/GaN HEMT surface on a large scale, as shown in Figs. 1(d) and 1(e). By modulating the Ga flux to avoid microcrystal formation, and by using T_{sub} of ~740 °C and an RF power of ~480 W, we realized smooth coalesced surfaces, as shown in Fig. 1(f). However, the Hall effect measurement in van der Pauw geometry at RT and 77 K showed a 2DEG mobility μ of ~530/950 $cm^2/V{\cdot}s$ and a density n_s of $\sim 2.0 \times 10^{13}/1.50 \times 10^{13}$ cm^{-2}. The relatively low 2DEG mobility, the significant difference in RT, and the 77 K charge density, which will manifest in severe buffer leakage (discussed later), are addressed in the subsequent epilayer growths.

Further improvements were thus made in the epitaxy: the AlN nucleation layer (~100 nm) was grown N_2-rich with a III/V ratio of ~0.9, a thicker 1.5 µm GaN buffer was employed, and Al predeposition prior to the AlGaN growth was performed to enhance the 2DEG mobility by reducing alloy scattering.[16] All these HEMT structures were capped with a 2-nm-thick GaN layer. A representative (002) X-ray diffraction pattern confirming the epilayer structures is shown in Fig. 2(a). The FWHM of the GaN peak measured from a (002) rocking curve was ~900 arcsec. The asymmetric scans resulted in FWHMs of ~2000 and ~2520 arcsec when the GaN peak was measured from (102) and (201) rocking curves, respectively. The uniformity of the grown film has been noted for the whole 3-in. Si wafer and is shown in Fig. 2(b). The schematic layer structure and the high-resolution transmission electron microscopy (HRTEM) image of the epilayer confirming the barrier thicknesses are also shown in the inset of Fig. 2(a), showing the successful realization of the desired heterostructure by MBE.

One of the key challenges to achieving high-performance DC and RF GaN devices on Si is to ensure low leakage (or high resistivity) in GaN buffer layers. The electronic conductivity of the GaN buffer layer in turn depends on the growth conditions of the AlN nucleation layer. For our initial growths as mentioned earlier, a significant difference between the RT and 77 K charge densities was observed, which is indicative of the freeze out of shallow dopants in a parallel conduction path through the buffer layer. Figure 3(a) shows the secondary ion mass spectrometry (SIMS) depth profile of the initial "1st-generation" AlGaN/GaN HEMTs. It illustrates significant incorporation of Si into the AlN and GaN layers. Although no silicon flux was used during the growth, the out-diffusion causes a silicon concentration of $\sim 2 \times 10^{20}$ cm^{-3} in the AlN layer and large spikes at the GaN/AlN interface. This conductive interface is responsible for conductive "buffer" leakage[17] currents in III–nitride HEMTs, affecting the speed and on/off ratio of the transistors significantly. During the AlN growth, the Si atoms float on the growth surface and reach the AlN/GaN interface. At the interface, Si becomes preferentially consumed into GaN instead of excess surface

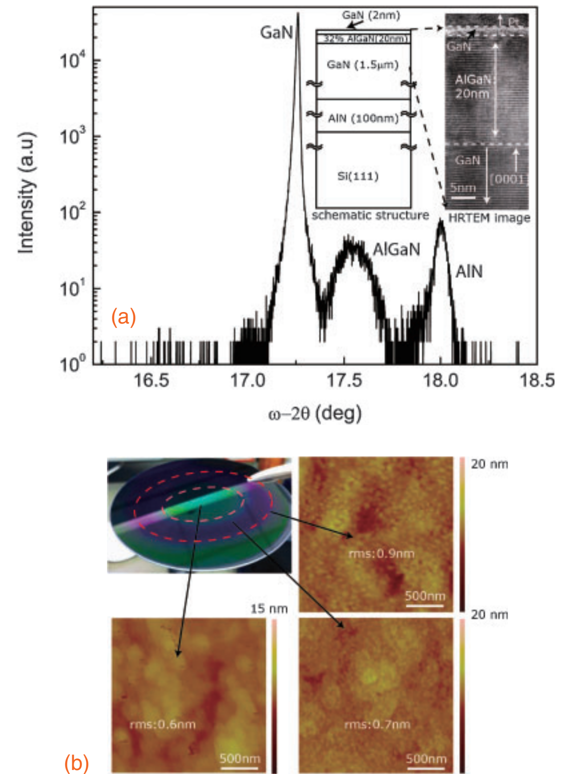

Fig. 2. (a) X-ray diffraction pattern of (002) ω–2θ scan for GaN (2 nm)/AlGaN (20 nm)/GaN (1.5 µm)/AlN (100 nm) HEMT epitaxial structure. The schematic layer structure and HRTEM image confirming the thicknesses are shown in the inset. (b) AFM image map of the grown AlGaN HEMTs on 3-in. HR-Si showing smooth surface morphologies and high uniformity.

Ga resulting in a large Si concentration spike.[18] The transport of Si through the AlN layer can be reduced significantly by incorporating N_2-rich AlN layers, as discovered previously for GaN growth on SiC substrates.[19] Thus, in our "2nd-generation" growths, we employed such a growth condition. Hall effect measurements at RT and 77 K showed a 2DEG mobility μ of ~1005/1815 $cm^2/V{\cdot}s$ and a density n_s of $\sim 1.44 \times 10^{13}/1.42 \times 10^{13}$ cm^{-2}. The R_{sh} at 300 K was measured to be 432 Ω/sq, which is among the best reported for AlGaN/GaN HEMTs on Si.[9] The fact that the sheet densities at 300 and 77 K 2DEG are nearly identical indicates the removal of parallel conducting channels. The SIMS profile of such samples in Fig. 3(b) shows much reduced Si incorporation in AlN, and more crucially, the removal of the Si spike at the AlN/GaN heterointerface. A similar strategy was also adopted in an earlier work on AlGaN HEMTs growth on Si.[20] However, in this work, we compare and correlate such a growth strategy with the subsequent improvement of device characteristics, as described next. To compare the buffer leakage, 100×100 μm^2 source/drain ohmic metal pads of Ti/Al/Ni/Au (20/100/40/50 nm) stacks were deposited on the 1st- and 2nd-generation HEMT samples with 2 µm separation. The subsequent anneal in N_2/Ar atmosphere for 16 s at 860 °C was carried out to ensure that the metals made ohmic contacts with the 2DEG at the AlGaN/GaN heterojunction. Prior to the ohmic process, mesa isolation was achieved with BCl_3/Cl_2 plasma reactive ion etching, and an etch depth of ~100 nm was obtained and verified. This etch process ensures the removal of the 2DEG channel, and now, any current (buffer leakage) between the pads flows only

© 2014 The Japan Society of Applied Physics

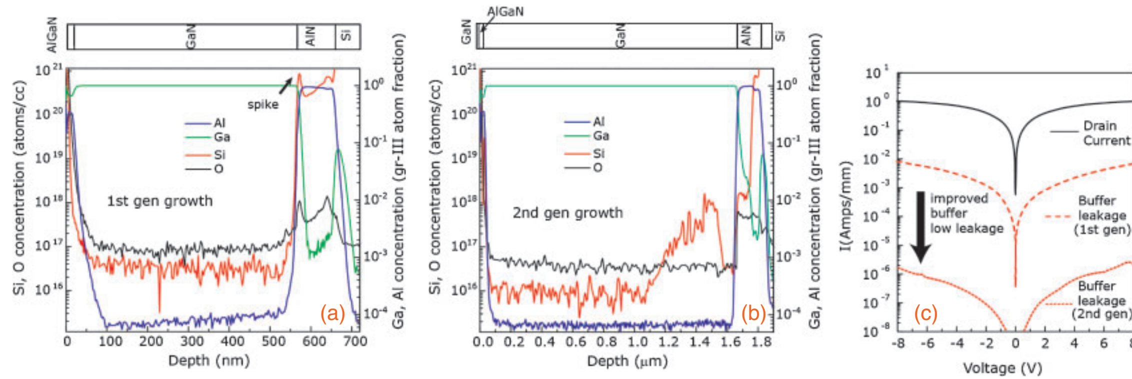

Fig. 3. (a) SIMS depth profiles of Al, Ga, Si, and O concentrations of the 1st-generation GaN HEMTs grown by plasma MBE on HR-Si. A large Si concentration spike is seen at the AlN/GaN interface. (b) The SIMS depth profile of the 2nd-generation HEMTs shows less Si in the AlN layer and the absence of the sharp Si spike at the AlN/GaN interface. (c) Comparison of the drain current through the 2DEG and the buffer leakage currents after removal of the 2DEG of the 1st- and 2nd-generation HEMTs.

through unintentional leakage paths. Figure 3(c) shows that the reduced Si spike results in a *significant* $\sim\times 10^4$ reduction of the buffer leakage current. For comparison, the drain current between TLM pads flowing through the 2DEG between ohmic pads with 2 μm separation is also presented. This improved buffer is the consequence of the N_2-rich AlN nucleation layer used during the growth of the 2nd-generation HEMTs. This finding is crucial for the realization of low-leakage MBE-grown GaN HEMTs on Si.

For superior device performance, MBE regrowth was performed for the ohmic source/drain contacts for the 2nd-generation HEMT samples. A SiO_2 mask was patterned on the sample for defining the n+ GaN ohmic regrowth region. Subsequently, the unmasked windows were etched ~50 nm using BCl_3 (30 sccm) gas at a 40 V DC voltage to remove the AlGaN barrier layer completely. The sample was then loaded in the MBE chamber, and ~100 nm heavily doped n+ GaN was regrown under a metal-rich growth condition at T_{sub} of ~660 °C. The Si doping density in the regrown contact region was $\sim 10^{20}$ cm^{-3}, as verified by SIMS calibration and transport data. Following regrowth, the poly-GaN deposited on top of the SiO_2 mask was lifted off with SiO_2 by BHF treatment. Nonalloyed Ti/Au (20/100 nm) stacks were then deposited in the n+ S/D regions followed by mesa isolation using Cl_2-based plasma etching. Finally, Ni/Au (40/100 nm) gate metal stacks were deposited on the epitaxial surface by e-beam evaporation without any additional gate dielectrics. The schematic of the finished device and the large-scale scanning transmission electron microscopy (STEM) image showing the epilayers along with the regrown ohmic and gate regions are shown in Fig. 4(a). The slanted etch profile of the SiO_2 sidewall ensured the smooth connection between the 2DEG and the regrown n+GaN S/D regions, as shown in the magnified HRTEM image in the same figure. This intimate contact of the regrown region with the slanted heterojunction sidewall is the key to reducing the total contact resistance R_c between the metal and the 2DEG.

Transmission-line method (TLM) measurements were used to investigate the electrical characteristics of the regrown n+GaN. The TLM gaps between regrown n+ GaN wells were measured by scanning electron microscopy (SEM). At 300 K, R_c of ~0.1 Ω·mm and R_{sh} of ~486 Ω/sq were extracted, as shown in Fig. 4(b). The sheet resistance of

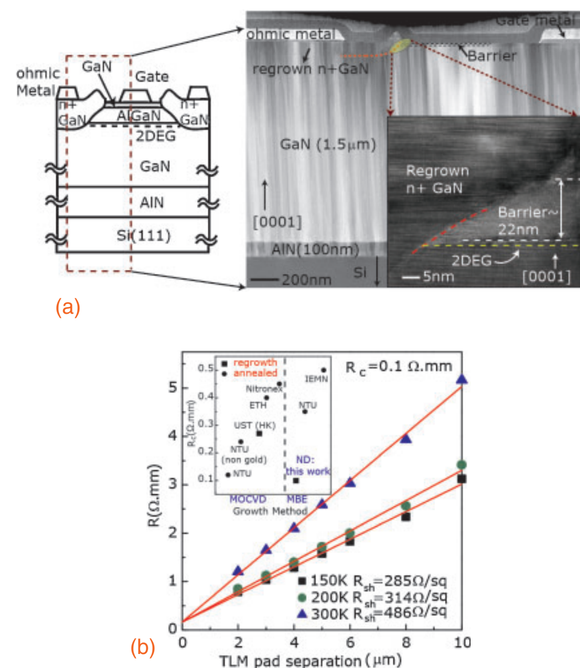

Fig. 4. (a) Schematic of the cross section of a processed HEMT with MBE-regrown source/drain contacts and the corresponding STEM image showing the epilayers along with the ohmic regrown regions and gate contacts. The magnified HRTEM image shows the smooth connection between the regrown epitaxial n+ GaN and the barrier layer. (b) Resistance between TLM pads for regrown ohmic contacts with AlGaN/GaN HEMT channels measured at 150, 200, and 300 K showing the temperature-independent low contact resistance. Benchmark plot of R_c for GaN HEMTs on Si grown by MBE and MOCVD is shown in the inset.

the completely processed sample is similar to that before processing. The R_c value is the lowest reported for GaN HEMTs on Si.[21,22] A benchmark plot has been provided in the inset of Fig. 4(b), which shows the R_c values reported by various groups for GaN HEMTs on Si grown by both MBE and MOCVD. From the temperature-dependent TLM plots shown in Fig. 4(b), it is seen that R_{sh} decreases from 486 Ω/sq at RT to 285 Ω/sq at 150 K. A similar trend was reported earlier for InAlN HEMTs on SiC.[23] This decrease is due to the increase in the mobility of the 2DEG owing to the reduction in polar optical phonon scattering at lower temperatures. The polarization-induced 2DEG density does

© 2014 The Japan Society of Applied Physics

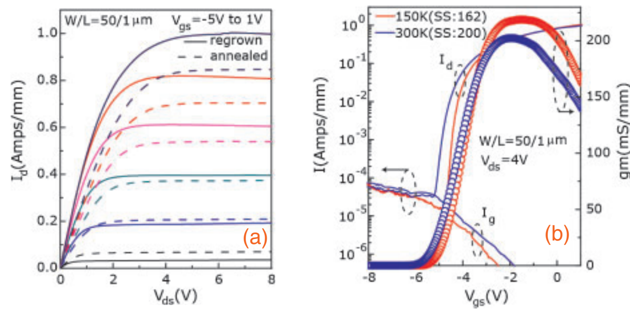

Fig. 5. (a) Room-temperature DC common source family of I_d–V_{ds} curves of the AlGaN/GaN HEMTs on Si with regrown ohmic contacts (solid) and annealed ohmic contacts (dashed). The MBE-regrown ohmic contacts result in a lower R_{on} and a higher output current density I_d. (b) Transfer (or switching) characteristics at 300 and 150 K for HEMTs with regrown ohmic contacts for $V_{ds} = 4$ V, and the transconductance as a function of gate voltage.

not change with temperature. On the other hand, as seen in Fig. 4(b), R_c is insensitive to temperature, thus supporting the earlier observation and possible explanations[23] as well.

To evaluate the effect of the regrown contacts on the device performance, the 2nd-generation HEMT sample processed using the regrown contact technique (described above) was compared with a sample from the same wafer but processed with an annealed ohmic. The annealed ohmic yielded R_c of ~0.6 Ω·mm. The DC common source characteristics of the two transistors fabricated using two different ohmic processes with identical L_g of ~1 µm, L_{sd} of ~2 µm, and width W of ~50 µm are shown in Fig. 5(a). The saturation drain current density I_{dsat} of the HEMTs with the regrown contacts was measured to be ~1.02 A/mm at $V_{gs} = 1$ V and R_{on} was 1.6 Ω·mm. Under similar bias conditions, I_{dsat} of ~0.85 A/mm and R_{on} of ~2.6 Ω·mm were measured for the HEMTs with annealed ohmic contacts. These results indicate that the low R_{on} and high I_{dsat} are consequences of the low R_c resulting from the regrown ohmic process. The high I_{dsat} and low R_{on} are attractive for high-power applications and for reducing losses in high-power and high-frequency microwave circuits.

The RT and 150 K DC transfer characteristics of the HEMTs with regrown contacts are shown in Fig. 5(b). $I_{ON}/I_{OFF} > 10^4$ was obtained for $V_{ds} = 4$ V. The peak extrinsic transconductances $g_{m,ext}$ of 205 and 225 mS/mm were measured at 300 and 150 K, respectively. The increase in g_m with the reduction in temperature is a consequence of the mobility boost owing to the low polar optical phonon scattering. The subthreshold slope (SS) does not scale as expected (kT/q) with temperature since the lowest currents are limited by gate leakage currents,[24] as shown in Fig. 5(b). The gate leakage is most likely dominated by the trap-assisted modified Frenkel–Poole emission[25] and the Fowler–Nordheim tunneling; it can be substantially reduced by the integration of Al_2O_3 or similar dielectrics. The DC and RF performance characteristics of submicron-gate-length (~75 nm) devices have been reported elsewhere.[26]

In conclusion, in this work, we report the MBE growth of GaN HEMTs on Si(111). The smooth surface morphology, low FWHM values of the AlN nucleation, low-leakage GaN buffer, and low R_{sh} of the resulting HEMTs indicate that the transport properties are among the lowest reported to date by MBE growth. The use of N_2-rich AlN nucleation solves the problem of buffer leakage and enables superior RF and DC performance. Superior device performance has been achieved by integrating MBE regrown ohmic contacts with GaN HEMTs on Si. This has resulted in the lowest R_c for GaN HEMTs on Si reported to date. Finally, with the very low contact resistance achieved in this work coupled with a thinner barrier and device scaling, a further boost in the performance of GaN HEMTs on Si is expected. These advances show MBE to be a capable and enabling technique for integrating RF and high-voltage functionalities to silicon, and to seed other functionalities that emerge from such integration.

1) M. A. Khan, A. Bhattarai, J. N. Kuznia, and D. T. Olson, Appl. Phys. Lett. **63**, 1214 (1993).
2) K. Shinohara, D. Regan, A. Corrion, D. Brown, Y. Tang, J. Wong, G. Candia, A. Schmitz, H. Fung, S. Kim, and M. Micovic, IEDM Tech. Dig., 2012, p. 27.2.
3) W. E. Hoke, R. V. Chelakara, J. P. Bettencourt, T. E. Kazior, J. R. LaRoche, T. D. Kennedy, J. J. Mosca, A. Torabi, and A. J. Kerr, J. Vac. Sci. Technol. B **30**, 02B101 (2012).
4) J. W. Chung, J.-K. Lee, E. L. Piner, and T. Palacios, IEEE Electron Device Lett. **30**, 1015 (2009).
5) R. K. Jana, G. L. Snider, and D. Jena, Phys. Status Solidi C **10**, 1469 (2013).
6) H. W. Then, S. Dasgupta, M. Radosavljevic, L. Chow, B. Chu-Kung, G. Dewey, S. Gardner, X. Gao, J. Kavalieros, N. Mukherjee, M. Metz, M. Oliver, R. Pillarisetty, V. Rao, S. H. Sung, G. Yang, and R. Chau, IEDM Tech. Dig., 2013, 28.3.1.
7) A. Watanabe, T. Takeuchi, K. Hirosawa, H. Amano, K. Hiramatsu, and I. Akasaki, J. Cryst. Growth **128**, 391 (1993).
8) F. Medjdoub, B. Gimbert, D. Ducatteau, and N. Rolland, Appl. Phys. Express **6**, 044001 (2013).
9) W. E. Hoke, T. D. Kennedy, J. J. Mosca, A. J. Kerr, A. Torabi, S. Davis-Hearns, and J. R. LaRoche, J. Vac. Sci. Technol. B **29**, 03C107 (2011).
10) K. Radhakrishnan, N. Dharmarasu, Z. Sun, S. Arulkumaran, and G. I. Ng, Appl. Phys. Lett. **97**, 232107 (2010).
11) J. Guo, Y. Cao, C. Lian, T. Zimmermann, G. Li, J. Verma, X. Gao, S. Guo, P. Saunier, D. Jena, and H. Xing, Phys. Status Solidi A **208**, 1617 (2011).
12) K. Shinohara, A. Corrion, D. Regan, I. Milosavljevic, D. Brown, S. Burnham, P. J. Willadsen, C. Butler, A. Schmitz, D. Wheeler, A. Fung, and M. Micovic, IEDM Tech. Dig., 2010, 30.1.1.
13) S. Dasgupta, Nidhi, D. F. Brown, F. Wu, S. Keller, J. S. Speck, and U. K. Mishra, Appl. Phys. Lett. **96**, 143504 (2010).
14) T. Huang, X. Zhu, and K. M. Lau, IEEE Electron Device Lett. **33**, 1123 (2012).
15) E. Calleja, M. A. Sanchez-Garcia, E. Monroy, F. J. Sanchez, E. Munoz, A. Sanz-Hervas, C. Villar, and M. Aguilar, J. Appl. Phys. **82**, 4681 (1997).
16) G. Li, Y. Cao, H. G. Xing, and D. Jena, Appl. Phys. Lett. **97**, 222110 (2010).
17) Y. Cao, T. Zimmermann, H. Xing, and D. Jena, Appl. Phys. Lett. **96**, 042102 (2010).
18) W. E. Hoke, A. Torabi, J. J. Mosca, and T. D. Kennedy, J. Vac. Sci. Technol. B **25**, 978 (2007).
19) W. E. Hoke, A. Torabi, R. B. Hallock, J. J. Mosca, and T. D. Kennedy, J. Vac. Sci. Technol. B **24**, 1500 (2006).
20) R. Aidam, E. Diwo, N. Rollbuhler, L. Kirste, and F. Benkhelifa, J. Appl. Phys. **111**, 114516 (2012).
21) S. Arulkumaran, G. I. Ng, S. Vicknesh, H. Wang, K. S. Ang, C. M. Kumar, K. L. Teo, and K. Ranjan, Appl. Phys. Express **6**, 016501 (2013).
22) S. Arulkumaran, S. Vicknesh, N. G. Ing, S. L. Selvaraj, and T. Egawa, Appl. Phys. Express **4**, 084101 (2011).
23) J. Guo, G. Li, F. Faria, Y. Cao, R. Wang, J. Verma, X. Gao, S. Guo, E. Beam, A. Ketterson, M. Schuette, P. Saunier, M. Wistey, D. Jena, and H. Xing, IEEE Electron Device Lett. **33**, 525 (2012).
24) J. W. Chung, J. C. Roberts, E. L. Piner, and T. Palacios, IEEE Electron Device Lett. **29**, 1196 (2008).
25) S. Ganguly, A. Konar, Z. Hu, H. Xing, and D. Jena, Appl. Phys. Lett. **101**, 253519 (2012).
26) S. Ganguly, B. Song, W. S. Hwang, Z. Hu, M. Zhu, J. Verma, H. G. Xing, and D. Jena, Phys. Status Solidi C **11**, 887 (2014).

© 2014 The Japan Society of Applied Physics